IEEE Access
Multidisciplinary | Rapid Review | Open Access Journal

Date of publication xxxx 00, 0000, date of current version xxxx 00, 0000.

Digital Object Identifier 10.1109/ACCESS.2017.Doi Number

Simulation of AC loss in the armature windings of a 100 kW all-HTS motor with various (RE)BCO conductor considerations

SHUANGRONG YOU[1], SWARN S. KALSI[2], (Life Fellow, IEEE), MARK D. AINSLIE[3], (Senior Member, IEEE), RODNEY A. BADCOCK[1], (Senior Member, IEEE), NICHOLAS J. LONG[1], ZHENAN JIANG[1], (Senior Member, IEEE)

[1]Robinson Research Institute, Victoria University of Wellington, Wellington, New Zealand
[2]Kalsi Green Power System, LLC Princeton, NJ 08540 USA
[3]Department of Engineering, University of Cambridge, Cambridge, UK

Corresponding author: Zhenan. Jiang (e-mail: zhenan.jiang@vuw.ac.nz).

XXXX.

ABSTRACT Superconducting machine designs have historically focused on an isolated, cryogenic rotor and conventional (copper) stator due to unacceptable levels of AC loss in a superconducting stator. Thus, AC loss reduction in the armature windings is one of the key issues for achieving practical all-superconducting motors that could deliver an unprecedented power density and significantly reduce machine complexity. In this paper, a 100 kW, 1500 rpm, all - HTS motor operating at 65 K is designed and AC loss simulations in HTS armature windings wound with different types of (RE)BCO conductor arrangements are carried out by implementing the ***T-A*** formulation and a rotating mesh using commercial FEM software COMSOL Multiphysics. Either 4 mm-wide (RE)BCO conductors, 14/2 (14 strands, each strand is 2 mm wide) (RE)BCO Roebel cables, or striated (RE)BCO conductors with four 1 mm-wide filaments are considered in the armature windings. The simulation results show that armature windings wound with Roebel cables or striated conductors can significantly reduce the AC loss in the armature windings compared to windings wound with 4 mm-wide conductors. It is also shown that the AC loss in the armature winding wound with the 4 mm-wide (RE)BCO conductors decreases with decreasing operating temperature. The AC loss reduction can be attributed to the reduced magnetic field penetration associated with the increased I_c in the winding. Finally, a 2% AC loss reduction can be achieved in the armature winding wound with (RE)BCO conductors with asymmetric I_c (B, θ) characteristics by simply flipping the direction of the conductors of the armature winding. The simulation results in this work have practical implications for designing all-HTS superconducting rotating machines. Such machines could be suitable for H_2 powered electric vehicles like large interstate trucks, heavy machinery, or locomotives.

INDEX TERMS FEM (finite element method), ***T-A*** formulation, high-temperature superconductors, all-superconducting motor, armature windings, AC loss, Roebel cables, striated conductors, asymmetric magnetic-field and field-angle dependent critical current

I. INTRODUCTION

High temperature superconducting (HTS) motors can provide higher efficiency and power density, with lower weight and smaller size compared with conventional copper wire-based rotating machines [1]. In an all-HTS motor, armature windings will carry AC currents under rotating magnetic fields generated by the field windings. The AC loss generated in the armature windings poses a major challenge to the cryogenic cooling system and techniques to reduce this AC loss in the armature windings must be developed in order to achieve practical fully - superconducting rotating machines.

The finite element method (FEM) has been widely used in modelling superconductors [2]–[9]. However, HTS motor modelling is a non-trivial task due to the rotating structure, non-linear resistivity, and high aspect ratio of HTS (RE)$Ba_2Cu_3O_{7-x}$ (hereinafter referred to as (RE)BCO, RE: rare earths) conductors. In 2018, hybrid models using mixed ***H***- and ***A***- formulation frameworks for modelling simple superconducting rotating machine examples were introduced in [10]. In these models, the superconducting coil windings were represented by simple rectangular or circular elements. Recently, more works simulating HTS machines have been

published [11]–[13], based on the ***T-A*** formulation as an alternative to the ***H-A*** formulation. The ***T-A*** formulation offers the advantage of easier implementation and faster computing time, treating the cross section of the (RE)BCO conductor as a 1D line [6]. In [11], a superconducting torque motor was designed for investigating the AC loss behaviour in the armature windings. Permanent magnets were used in the rotor to generate the rotating magnetic field. In [12], an AC loss model for one pole pair of a 10 MW generator was built based on ***T-A*** formulation. In [13], the ***T-A*** formulation was utilised for simulating the electromagnetic behaviour of the whole armature winding of a four-pole all-HTS generator. The simulation results using ***T-A*** formulation have close agreement with the simulation results using different methods [11].

However, in the modelling works mentioned above, only simple (RE)BCO tape arrangements were used in the armature windings and the AC loss behaviour in armature windings wound with low-loss conductor arrangements such as Roebel cables [14]–[18] and striated (RE)BCO conductors [19]–[23] have not yet been investigated. In addition, previous studies have reported an AC loss reduction in HTS coils wound with (RE)BCO conductors by simply varying the direction of the conductors in the coil windings [24]–[26]. The authors attributed the loss reduction to the asymmetric I_c (B, θ) characteristics of the (RE)BCO conductors, where field angle θ is defined as the angle between the normal vector of the conductor face and the magnetic field with respect to the current direction, as shown in Fig. 1(a). However, the influence of asymmetric I_c (B, θ) characteristics of (RE)BCO conductors in HTS armature windings under rotating magnetic fields have also not yet been studied.

In this paper, a 100 kW, 1500 rpm HTS motor is designed and 2D simulations of the AC loss in the HTS armature windings are carried out using the ***T-A*** formulation and a rotating mesh, implemented in COMSOL Multiphysics. The cross-section of the HTS motor is shown in Fig. 2 and the main parameters of the HTS motor are listed in Table I. The detailed calculation of the parameters in Table I is described in the Appendix. This motor is iron dominated just like conventional machines. However, replacing copper coils with superconducting coils reduces needed cross-sectional space for the coils with associated benefit of reduced iron core size and mass. The losses associated with the superconducting coils are a small fraction of losses in the copper coils. Since all superconducting coils and iron core operate at the same cryogenic temperature (LN2 or LH2), significant thermal load due to iron core losses becomes unattractive to remove with refrigerators. Such machines are expected to be suitable for applications where a cooling penalty is absent. Such applications include pumping of liquid cryogens (LN2 and LH2), H_2 powered electric vehicles like large interstate trucks, heavy machinery, and locomotives.

This work firstly explores the AC loss behaviours of the HTS armature windings for three different (RE)BCO conductor arrangements: 4 mm-wide (RE)BCO conductors; 14/2 (fourteen 2 mm wide strands) (RE)BCO Roebel cables; striated (RE)BCO conductors with four 1 mm-wide filaments. The schematic drawing of the three types of conductor arrangements are shown in Fig. 3. For the HTS armature windings wound with 4 mm - wide (RE)BCO conductors, the AC loss at different operating temperatures is calculated to explore its dependence on the operating temperature. Furthermore, the influence of the (RE)BCO conductor I_c (B, θ) characteristics on the AC loss in the armature winding is investigated when wound with SuperPower SCS (Surround Cu Stabilizer) 4050 AP (artificial pinning) (RE)BCO conductors which exhibit strong I_c (B, θ) asymmetry. The magnitude of the AC loss as well as current density and magnetic field distributions for the different armature windings are compared and discussed.

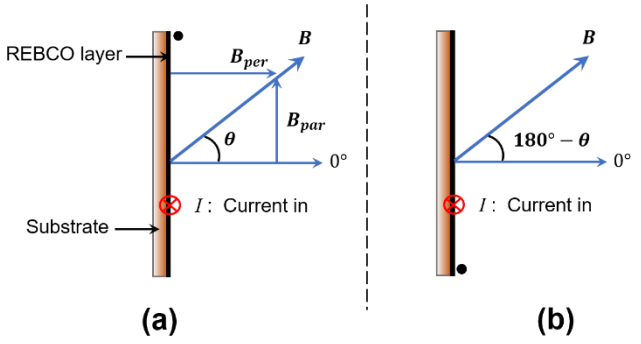

FIGURE 1. Relationship between the field angle, current direction, perpendicular component (B_{per}) and parallel component (B_{par}) of the external magnetic field: (a) definition of field angle θ; (b) definition of field angle after flipping the (RE)BCO conductor. The black dot is used to indicate the orientation of the (RE)BCO conductor.

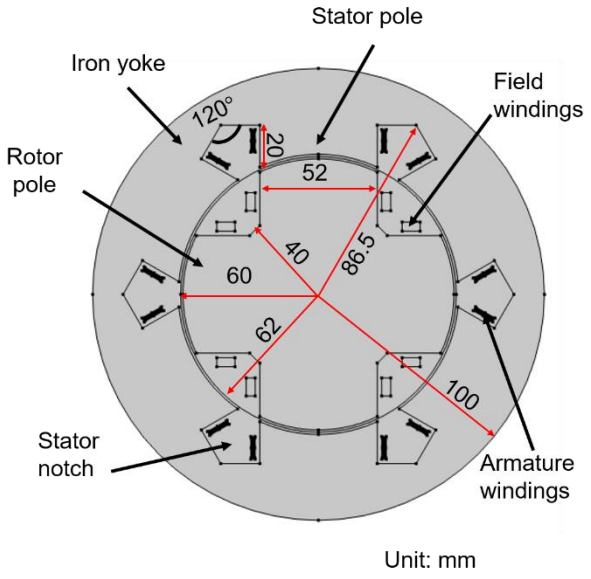

FIGURE 2. Cross-section of the 100 kW 1500 rpm all-HTS motor. All dimensions are given in mm.

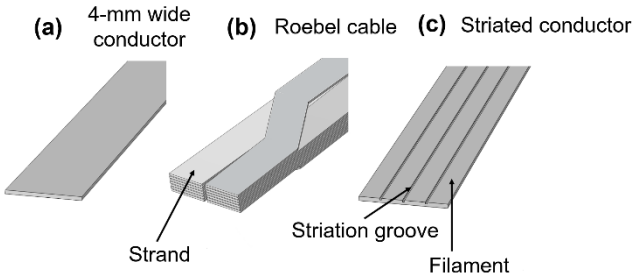

FIGURE 3. The three types of (RE)BCO conductor arrangements used in the numerical models: (a) 4 mm-wide (RE)BCO conductor, (b) 14/2 (fourteen 2 mm-wide strands) Roebel cable, (c) striated (RE)BCO conductor with four 1 mm-wide filaments.

TABLE I
KEY PARAMETERS OF THE HTS MOTOR

Parameters	Value
Output power (kW)	100
Rotating speed (rpm)	1500
Operating temperature (K)	65
Self-field I_c of the (RE)BCO conductors at 65 K (A/cm)	765
Ampere-turns (AC) per armature coil (kAt)	1.5
Frequency of armature current (Hz)	50
Ampere-turns (DC) per field coil (kAt)	4.0
Number of poles	4
Outer radius of the stator core (mm)	100
Inner radius of the stator core (mm)	62
Outer radius of the rotor core (mm)	60
Active length of the motor (mm)	300
Rotor pole width (mm)	52
Rotor pole length (mm)	24
Stator pole length (mm)	20
Stator notch width (mm)	11
Air gap (mm)	2
Radius to notch corner (mm)	86.5
Material of iron core and yoke	Silicon steel (non-grain oriented) M-36

II. NUMERICAL MODELLING

In this section, the modelling framework for the FEM models implemented in COMSOL Multiphysics is described. COMSOL's "Rotating Machinery" interface is used for implementing the ***A***-formulation and the "Coefficient Form Boundary PDE" interface is used for implementing ***T***-formulation. The *B-H* curve of the iron core and yoke (Non-grain-oriented silicon steel M-36) is imported from COMSOL's material database.

A. T-A FORMULATION

In the ***T-A*** formulation [6], the magnetic vector potential ***A*** is applied to the whole model, including the superconducting tape and other subdomains, while the current vector potential ***T*** is used only for computing the current density distribution in the superconducting layers. As shown in Eq. (1), current density ***J*** in the superconductor layers is defined as the curl of the current vector potential ***T***, which is always perpendicular to the conductor surface.

$$\boldsymbol{J} = \nabla \times \boldsymbol{T} = \left(\frac{\partial T_z}{\partial y} - \frac{\partial T_y}{\partial z}\right)\boldsymbol{i} + \left(\frac{\partial T_x}{\partial z} - \frac{\partial T_z}{\partial x}\right)\boldsymbol{j} + \left(\frac{\partial T_y}{\partial x} - \frac{\partial T_x}{\partial y}\right)\boldsymbol{k} \quad (1)$$

where T_x, T_y *and* T_z are the x, y and z component of ***T*** in Cartesian coordinates, as defined in Fig. 4.

In the 2D FEM model, the variable in "Coefficient Form Boundary PDE" interface is $|\boldsymbol{T}|$, which is a scalar. The direction of ***T*** is given by multiplying the unit normal vector, which is always perpendicular to the (RE)BCO conductor surface – see Fig. 4(a). The thickness of the (RE)BCO conductors is ignored and all conductors are simplified as 1D lines. ***J*** in the (RE)BCO conductors has only a *z*-component and ***T*** has only *x* and *y* components in the 2D plane. Thus, Eq. (1) can be written as Eq. (2) in the FEM model.

The operating current in each (RE)BCO conductor is equal to the circulation line integral of ***T*** as shown in Fig. 4(b). Thus, the edge constraints for defining the operating current can be written as Eq. (3).

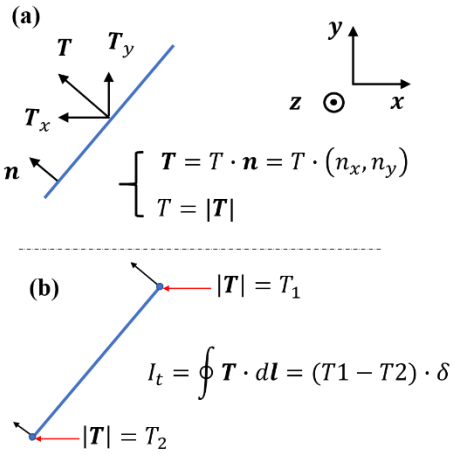

FIGURE 4. (a) Definition of the current vector potential *T* of the superconductor and (b) the boundary condition for the applied current.

$$|\boldsymbol{J}| = J_z = \frac{\partial T \cdot n_y}{\partial x} - \frac{\partial T \cdot n_x}{\partial y} \quad (2)$$

$$T_1 - T_2 = \frac{I_t}{\delta} \quad (3)$$

where n_x and n_y are the x and y components of the unit normal vector of the (RE)BCO conductors. T_1 and T_2 are the values of $|\boldsymbol{T}|$ on the edges as shown in Fig. 4(b). I_t is the forced transport current flowing in the (RE)BCO conductors and δ is the thickness of the superconducting layer which is set as 1 μm.

B. ROTATING MESH AND 2D MOTOR MODELS

A rotating mesh is applied to the rotor (see Fig. 5) to rotate the magnetic field generated by the rotor windings. In the armature windings, each 4 mm - wide conductor in the windings is divided into 60 mesh elements. A gradient mesh is applied in the (RE)BCO conductors for increasing the mesh density at the edges of the conductors.

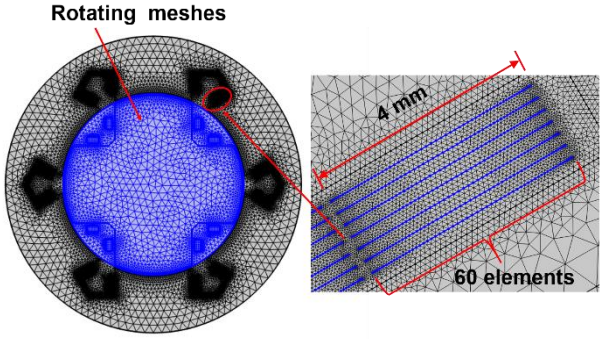

FIGURE 5. A moving mesh applied to the rotor part including rotor core, field windings and some air subdomains. A gradient mesh is applied to the edges of the (RE)BCO conductors.

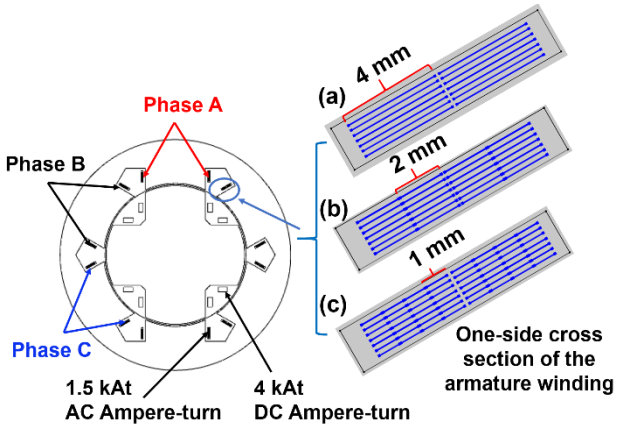

FIGURE 6. Schematic of the three different types of armature windings under investigation and the definition of the phases in the motor: (a) 4 mm-wide conductor; (b) 14/2 Roebel cable; (c) striated conductor. The ampere-turns of the armature windings are 1.5 kAt (AC) while the ampere-turns of the field winding is 4 kAt (DC). The phase difference of the current for different phase in the armature winding is $\frac{2}{3}\pi$.

Although the four field coils shown in Fig. 2 are designed with 4 mm - wide (RE)BCO conductors in the FEM model, they are treated as carrying homogenous DC currents in a 4 mm × 8 mm rectangular block. The AC loss behaviour in the field coils are not considered in this work. The field coils are defined using the "homogenized multiturn coil" node in the "Rotating machinery" interface. Each field coil has 28 turns and each turn carries a 142.9 A DC current, giving a total of 4 kAt. The armature winding is comprised of six double-racetrack coils wound around the iron stator poles and two serial-connected coils spatially facing each other form a phase (A, B, or C) as shown in Fig. 6. The enlarged cross-sections in Fig. 6 show one leg of the double-racetrack coil in Phase C wound with different (RE)BCO conductors. The distance between the neighbouring superconducting layers is 250 µm considering the non-superconducting layers and insulation thickness. All three cases use the same quantity of superconductor: in case (a), the double-racetrack coils are wound with 4 mm-wide (RE)BCO conductors and have 14 turns in total; in case (b), the double-racetrack coil is wound with a single 14/2 (fourteen 2 mm-wide strands) Roebel cable, hence have two turns; and in case (c), the double-racetrack coil is wound with 4-filament striated (RE)BCO conductors and have the same number of turns as case (a). The horizontal gap between the strands in the Roebel cable is 50 µm. Each striated conductor has four 1 mm-wide filaments and three 50 µm-wide grooves which separate the filaments. Here, we assume the striation can be achieved by laser ablation [27]. Coupling between the filaments is not considered in this work [20]. The ampere-turns per armature winding for all three different cases in this study is 1.5 kAt.

In the simulation, Roebel cables are simulated as two parallel stacks carrying the same current in each Roebel strand [14], [15]. Equal current is assumed in the striated conductors. Therefore, each double racetrack coil wound with Roebel cables and striated conductors is equivalent to a stack of two double racetrack coils wound with 2 mm conductors and a stack of four double racetrack coils wound with 1 mm conductors, respectively.

C. INTERPOLATION OF ANGULAR MAGNETIC FIELD DEPENDENCE OF CRITICAL CURRENT

The *E-J* power law and Ohm's law in Eq. (4) [28] and Eq. (5) are used in the FEM models for simulating the electromagnetic behaviour of the (RE)BCO conductors, specifically their nonlinear resistivity.

$$E = E_c \cdot \left(\frac{J}{J_c(B,\theta)}\right)^n \quad (4)$$

$$\boldsymbol{E} = \rho_{HTS} \cdot \boldsymbol{J} \quad (5)$$

where E_c is the characteristic electric field 1 µV/cm, n is the exponent of the *E-J* curve defining the steepness of the transition between the superconducting and normal state which is assumed to be 21, $J_c(B, \theta)$ is the angular magnetic field-dependent critical current density of the (RE)BCO conductors derived from measured $I_c(B, \theta)$ values divided by the cross-section of the (RE)BCO conductors. ρ_{HTS} is the non-linear resistivity of (RE)BCO conductors determined from Eq. (4).

(RE)BCO conductors from Shanghai Superconductor are considered for the AC loss calculation in the armature windings wound with different types of (RE)BCO conductors. The specifications of the HTS wires are listed in Table II. The $I_c(B, \theta)$ data shown in Fig. 7 are used to obtain the $J_c(B, \theta)$ values used in the simulations. In Fig. 7, the values between 0° and 180° are the measured data using the SuperCurrent system at the Robinson Research Institute, Victoria University of Wellington [29] and symmetry is assumed for the data from 180° to 360°. The baseline simulations in this work assume an operating temperature 65 K and hence Fig. 7(a) is used for

these simulations. Isothermal conditions are assumed, i.e., a constant temperature. Figs. 7 (b), (c), and (d) are used in the latter part of the paper for investigating the temperature dependence of the AC loss in the armature winding wound with 4 mm - wide (RE)BCO conductors.

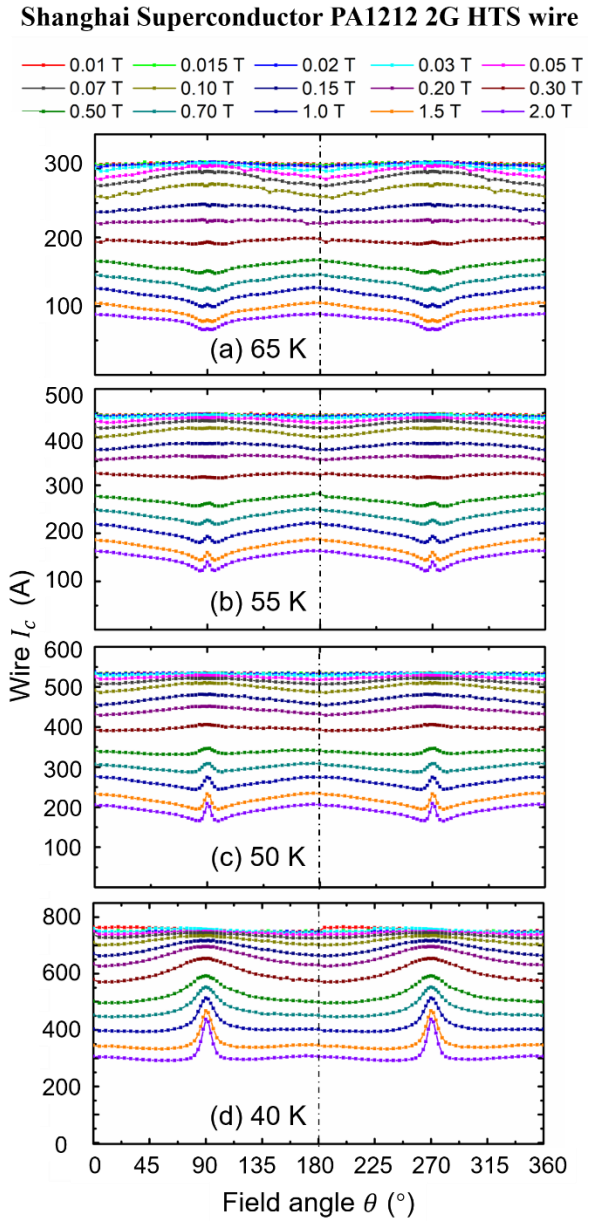

FIGURE 7. The measured I_c (B, θ) data used in the FEM models to represent the angular magnetic field-dependence of the critical current density. Symmetry is assumed for the data from 180° to 360°.

A direct interpolation of a three-column look-up table [B_{per}, B_{par}, $J_c(B_{per}, B_{par})$] is used to include this J_c (B, θ) dependence, where B_{per} and B_{par} are the perpendicular and parallel components of the magnetic field to the (RE)BCO conductor surface. B_{per} and B_{par} are given by Eq. (6) and Eq. (7).

$$B_{per} = \boldsymbol{B} \cdot \boldsymbol{n} = (B_x, B_y) \cdot (n_x, n_y) \quad (6)$$

$$B_{par} = \boldsymbol{B} \cdot (\boldsymbol{R}_{\frac{\pi}{2}} \boldsymbol{n}) = (B_x, B_y) \cdot (-n_y, n_x) \quad (7)$$

where B_x and B_y are the x and y components of the magnetic field in Cartesian coordinates, $\boldsymbol{n}$ is normal vector to the conductor surface, and $\boldsymbol{R}_\theta$ is the rotation operator given by Eq. (8).

$$\boldsymbol{R}_\theta = \begin{bmatrix} \cos\theta & -\sin\theta \\ \sin\theta & \cos\theta \end{bmatrix} \quad (8)$$

TABLE II
PARAMETERS OF THE 4 MM (RE)BCO CONDUCTORS

Parameters	value
Superconducting layer thickness(μm)	1
Conductor width (mm)	4
Conductor thickness (μm)	100
Conductor thickness after insulation (μm)	250
Substrate material	Hastelloy
I_c (self-field, 77.5 K)	145 A

III. SIMULATION RESULTS AND DISCUSSION

The models in this work are a 2D representation of the cross-section of the HTS motor. Thus, end effects (i.e., the winding heads) in the armature windings are not considered. The AC loss values in the armature windings are obtained from the 2D results per unit length multiplied by the effective length of the coil windings. The number of DOFs (degrees of freedom) and computing time for the three models wound with different (RE)BCO conductors for one rotational period (40 ms) are listed in Table III. The PC used in this work has a 3.7 G Hz CPU (Intel(R) Xeon(R) W-2135) and 64 GB RAM.

TABLE III
COMPUTING PARAMETERS OF THREE FEM MODELS

Types of armature winding	DOF	Computing time (hr)
4 mm conductor	9.7 k	11.5
Roebel cable	10.5 k	14
Striated conductor	15.4 k	22

A. LOSS COMPARISON IN HTS ARMATURE WINDINGS WOUND WITH THREE TYPES OF (RE)BCO CONDUCTORS

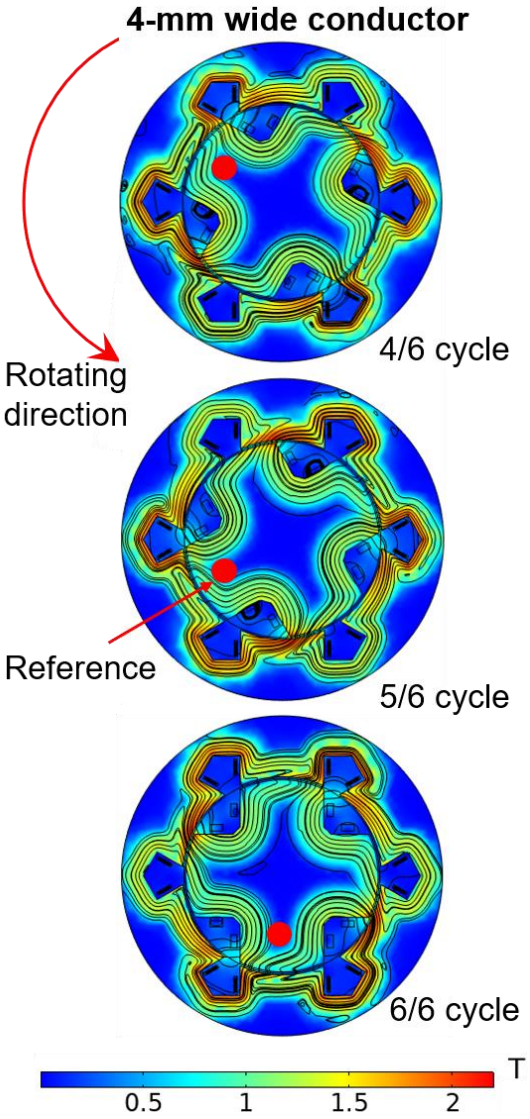

FIGURE 8. Magnetic field distributions in the motor at *t* = 4/6 cycle, *t* = 5/6 cycle and *t* = 6/6 cycle. The conductors used in the armature winding here are 4 mm - wide (RE)BCO conductors. The distributions derived from the other two FEM models using Roebel cables and striated conductors are very similar to that shown here.

The magnetic field distributions of the HTS motor wound with the 4 mm - wide (RE)BCO conductor at 4/6 cycle, 5/6 cycle and 6/6 cycle are shown in Fig. 8. In order to avoid the influence of transient results associated with the virgin magnetisation state, the results shown in Fig. 8 start from 4/6 cycle. The pattern of the magnetic field distributions remains the same for all different moments, except for the counter - clockwise rotation associated with rotation of the rotor. Every 1/6 cycle the field distribution is repeated but is rotated by 60°. Although the maximum magnetic field in the motor is approximately 2.2 T, the field at the armature windings is lower than 0.5 T because the magnetic flux is concentrated in the iron poles and yokes due to their high permeability.

These results indicate that the electromagnetic behaviour of each coil winding is equivalent but with a 60° phase difference. Therefore, because of this symmetry, we can choose any coil winding to analyse the AC loss behaviour and translate this to the whole armature winding.

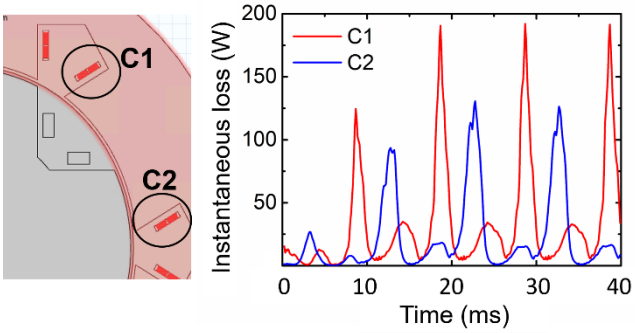

FIGURE 9. C1 and C2: two legs of one armature coil. The calculated instantaneous losses of C1 and C2 wound with 4 mm - wide (RE)BCO conductors are shown.

Although the AC loss behaviour of each double-racetrack coil are equivalent, there is difference in the AC loss behaviour of each leg (straight part) of the coil. As shown in Fig. 9, C1 and C2, which are the two legs of a double-racetrack coil, exhibit different instantaneous loss characteristics. The different instantaneous loss curves of C1 and C2 in the plot arise from the fact that C1 and C2 experience a different magnetic field from the rotor and carry opposite currents. In the following, C1, which has a higher instantaneous loss than C2, is chosen for analysing the loss behaviour in more detail.

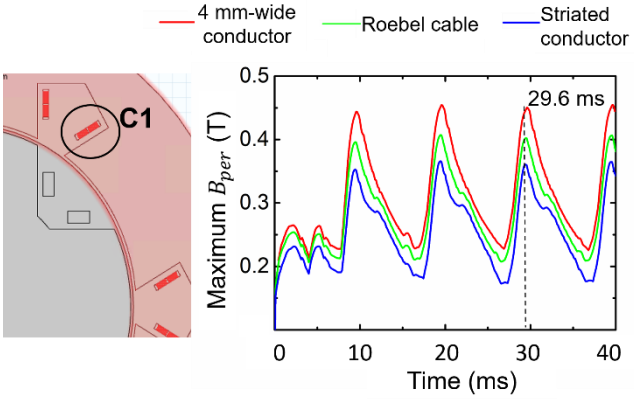

FIGURE 10. Maximum perpendicular component of the magnetic field in C1 for three different types of armature winding as a function of time.

Fig. 10 shows the periodic maximum perpendicular component of the magnetic field (hereafter referred to as B_{per}) in C1 wound with the three different (RE)BCO conductor arrangements. The period of maximum B_{per} is 10 ms, which is 1/4 of the rotational period of the rotor and the maximum B_{per} value occurs at 29.6 ms. The peak values of B_{per} for the three

cases are 0.45 T, 0.40 T and 0.36 T, respectively. The maximum value of B_{per} in windings is an indirect reflection of the magnitude of the AC loss in the coil windings because B_{per} contributes the most to AC loss in (RE)BCO conductors [30]. The results in Fig. 10 show that Roebel cable and striated conductor reduce the maximum B_{per} in the windings.

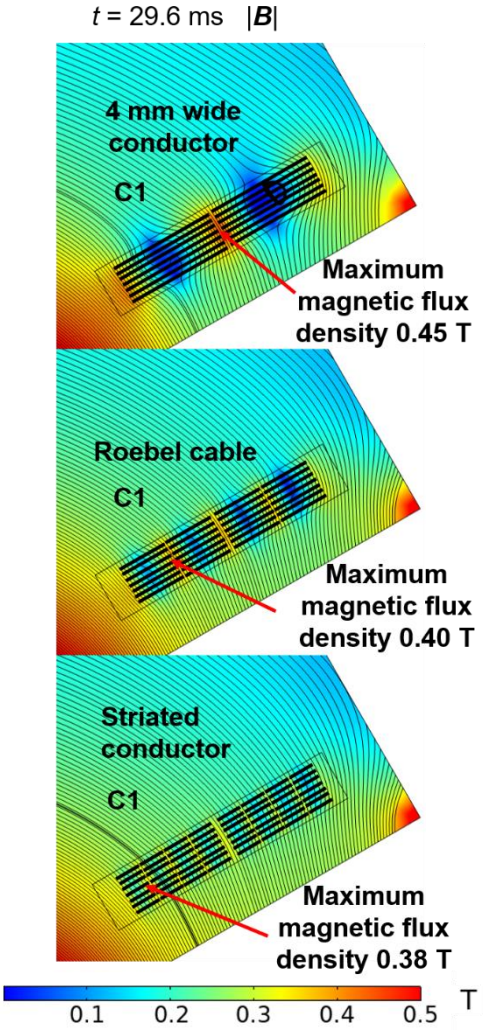

FIGURE 11. Magnetic flux density distributions and flux lines in C1 wound with three types of (RE)BCO conductor arrangements at t = 29.6 ms. The thickness of the superconductor layer is artificially enlarged here for clarity.

Fig. 11 shows the magnetic flux density distribution and flux lines around C1 at t = 29.6 ms. The magnetic field density is the highest near the airgap for all the three cases. Flux-free regions exist in the middle of each racetrack coil wound with the 4 mm-wide (RE)BCO conductors and Roebel cables, as shown in Figs. 11(a) and (b). In both cases, the flux-free region becomes smaller closer to the airgap. The existence of the flux-free region is due to the shielding current in the racetrack coils which repels the external magnetic field from the rotor. The magnetic field is concentrated in the gaps annotated by red arrows. This is caused by the superposition of the magnetic field generated by the shielding current and the external magnetic field from the rotor. The maximum magnetic flux density in C1 wound with 4 mm-wide conductors, Roebel cables, and striated conductors are 0.45 T, 0.40 T and 0.38 T, respectively. These values are very close to the maximum B_{per} values at 29.6 ms. This indicates the magnetic field is mostly perpendicular to the (RE)BCO conductors.

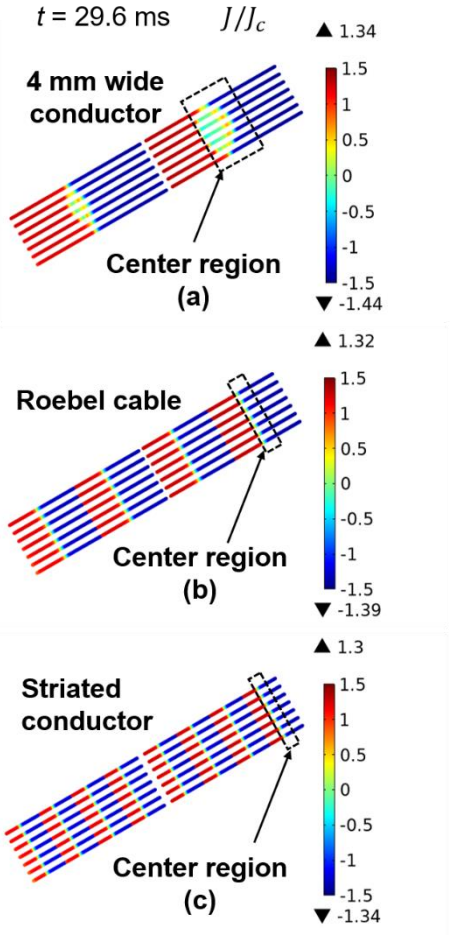

FIGURE 12. Normalized current density J/J_c distributions in C1 wound with three types of (RE)BCO conductor arrangements at t = 29.6 ms at the rated current.

Fig. 12 shows the normalized current density J/J_c distributions for the three cases in C1 at 29.6 ms at the rated current. In Section II. 2, it was mentioned that each double racetrack winding wound with Roebel cables and striated conductors is equivalent to a stack of two double racetrack coils wound with 2 mm conductors and a stack of four double racetrack coils wound with 1 mm conductors, respectively. In all cases, shielding currents in the conductors repel the external magnetic field which is consistent with the magnetic field distribution in Fig. 11. It is worth noting that the magnetic flux is fully penetrated in the regions where $|J/J_c|>1$ and the AC loss is mainly generated in these regions. There exists current-free regions ($|J/J_c|\sim 0$) near the centre of each equivalent racetrack coil denoted in the rectangular boxes in the figure

and it is most obvious in C1 wound with the 4 mm-wide (RE)BCO conductor. The current-free regions correspond to the flux-free regions in Fig. 11. It can be seen that the blue-filled region in each equivalent racetrack coil is larger than that of the red-filled region which means the net current at this moment is negative and is flowing near the central region. The maximum value of $|J/J_c|$ for the three cases are 1.44, 1.39 and 1.34, respectively.

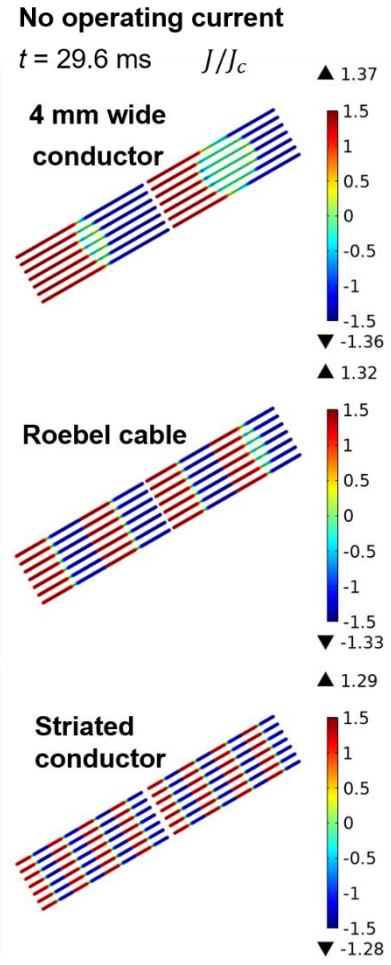

FIGURE 13. Normalized current density J/J_c distribution in C1 wound with three types of (RE)BCO conductor arrangements at t = 29.6 ms, without any operating current, i.e., no net transport current.

Fig. 13 shows the normalized current density J/J_c distributions for the three cases in C1 at 29.6 ms when the coils carry zero net transport current. In this situation, only shielding currents flow in the windings due to the external magnetic field from the rotor. The current density distributions closely resemble those in Fig. 12 where net transport current flows in the middle of the equivalent coils. The difference between the current density distributions in Figs. 12 and 13 gives a clear idea of where the transport current flows. The result in Fig.13 implies that magnetization loss due to shielding current caused by the rotating field dominates the total AC loss in the armature windings. The difference in the size of the current-free (or flux-free) region in the two racetrack coils wound with 4 mm-wide conductor is due to the difference in the magnetic field around C1. Although a current-free region does exist in small central regions in C1 wound with 4 mm-wide conductors and Roebel cables, most regions in C1 wound for all the conductor arrangements are filled with saturated shielding current ($|J/J_c| > 1$) due to the rotating magnetic field. In other words, the magnetic field is almost fully penetrated in each conductor. When the external magnetic field is fully penetrated, the magnetization AC loss is proportional to the amplitude of the external magnetic field and the conductor width, and hence the magnetization loss in the armature windings could be reduced by the use of narrow low-loss Roebel cables and striated conductors [31], [32] . Because the magnetization loss is the dominant loss component, this would reduce the total AC loss in the armature windings.

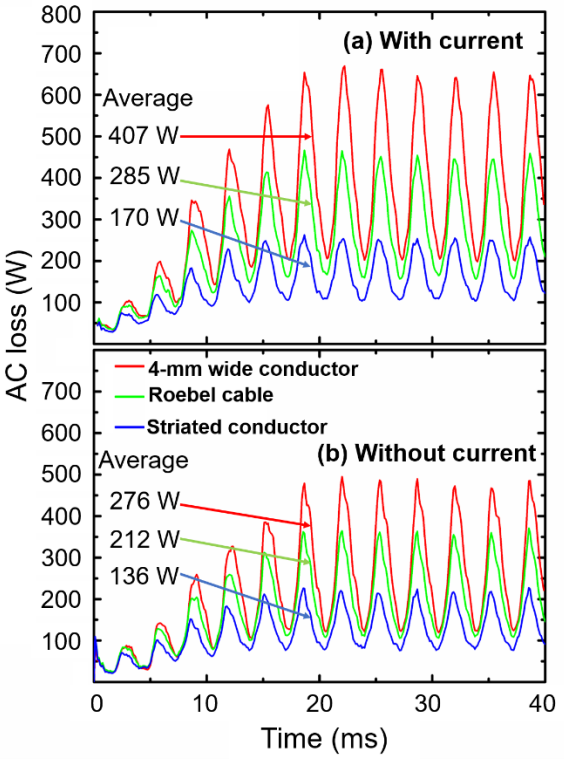

FIGURE 14. Comparison of the instantaneous AC loss in the armature windings wound with three types of (RE)BCO conductor arrangements: (a) at the rated current; (b) with zero net transport current.

Fig. 14 (a) compares the instantaneous loss in the armature windings wound with three different (RE)BCO conductor arrangements when the armature carries the rated current. The result shows the total AC loss considering all six coils of the armature. The average total AC loss values for armature windings wound with the 4 mm-wide conductor, 14/2 Roebel cable, and the 4-filament striated conductors are 407 W, 285 W, and 170 W, respectively. This total loss result shows a significant AC loss reduction can be achieved by using Roebel cables or striated conductors in the armature windings. Compared with the armature winding wound with 4 mm-wide

conductors, the average AC loss in armature windings wound with Roebel cables and striated conductors is reduced by approximately 30% and 58%, respectively.

Fig. 14 (b) compares the instantaneous loss of the armature windings wound with the three different (RE)BCO conductor arrangements when the coils carry zero net transport current. In this case, the AC loss in the armature windings is purely the magnetization loss. The average values of the magnetization loss for the 4 mm-wide conductor, 14/2 Roebel cable, and the 4-filament striated conductor arrangements are 276 W, 212 W and 136 W, respectively. Again, a large reduction in the magnetization loss is observed for the Roebel cable and striated conductor arrangements. The result is consistent with the previous discussion related to Fig. 13. The magnetization loss values are 68%, 74% and 80% of the total loss, respectively. The result shown in Fig.14 provides additional evidence that magnetization loss dominates the total loss in the armature windings.

B. AC LOSS DEPENDENCE ON OPERATING TEMPERATURE

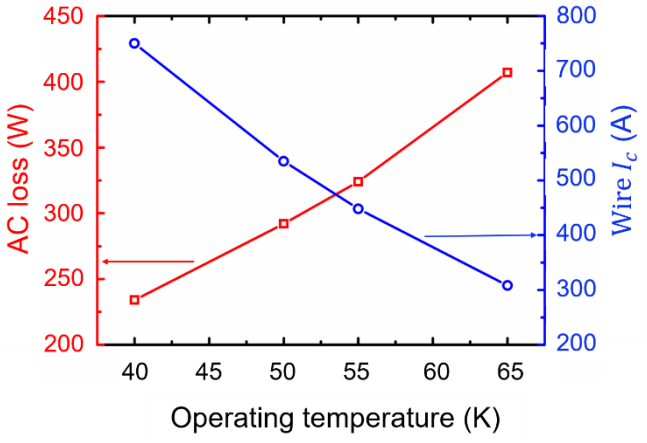

FIGURE 15. Temperature dependence of the AC loss in the armature winding wound with 4 mm-wide conductor and the temperature dependence of the self-field critical current of the (RE)BCO conductor.

In Fig. 15, the AC loss values in the armature winding wound with a 4 mm-wide (RE)BCO conductor are plotted as a function of operating temperature over the temperature range of 40 K – 65 K. The self-field critical current of the 4 mm - wide (RE)BCO conductor is also plotted in the figure. The average AC loss in the armature winding decreases with decreasing operating temperature, while the self-field critical current of the conductor increases with decreasing operating temperature. The AC loss characteristics can be attributed to the change of the effective penetration field in the coil windings due to the change of operating temperature and its influence on the flux pinning properties of the superconductor.

In Fig. 16, the theoretical magnetization loss curves under a perpendicular AC magnetic field derived by Brandt and Indenbom for a single (RE)BCO conductor used in this work at 65 K and 40 K are plotted as a function of the magnetic field amplitude [32]. 308 A and 750 A – the self-field I_c values of the 4 mm (RE)BCO conductor at 65 K and 40 K – are assumed in the calculation. There is a crossover magnetic field, $B_{crossover}$, at which the magnetization loss values are equal for different critical current values. Therefore, the magnetization loss in the conductor with a higher I_c are lower than those in the conductor with a lower I_c when the magnetic field is lower than $B_{crossover}$ as shown in Fig. 16. This phenomenon is due to the increase of the effective penetration magnetic field in the higher I_c conductor, i.e. the effective penetration field shifts towards higher magnetic field as depicted in Fig. 16. We can expect a similar behaviour in multi-turn armature coil windings. For HTS windings wound with many turns of (RE)BCO conductor, the penetration magnetic field increases due to a higher shielding ability at a given operating temperature [33], [34]. With decreasing the operating temperature, penetration magnetic field increases further due to the increase in I_c. Therefore, $B_{crossover}$ in (RE)BCO coil windings under AC magnetic fields is much larger.

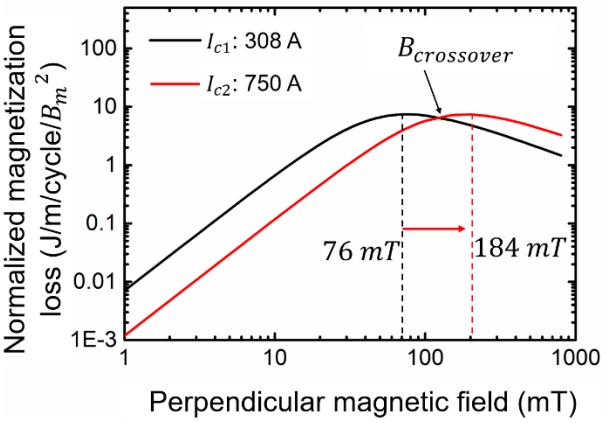

FIGURE 16. Normalized theoretical magnetization loss curves for the 4 mm-wide (RE)BCO conductor used in the FEM model at 65 K and 40 K. The magnetization loss values are equal for different I_c values when external magnetic field is $B_{crossover}$ [32].

Fig. 17 compares the normalized current density, J/J_c in C1 at 65 K and 40 K. Both racetrack coils at 65 K are almost fully penetrated while the flux penetration is limited to the edges of the coils at 40 K. The result implies that effective penetration field for the coils at 40 K is much greater than the effective penetration field of a single conductor at 40 K (184 mT, as shown in Fig. 16) and larger than 0.45 T which is the maximum perpendicular magnetic field component shown in Fig. 10. This proves the point made above regarding Fig. 16. The AC loss in the armature winding will decrease with a lower operating temperature because the effective penetration field for the coils will increase with decreasing operating temperature. However, one should be aware of a higher cooling penalty at lower operating temperatures. If the motor is a liquid hydrogen pump operated at 20 K where the cooling is "free" then this has practical implications on its efficiency.

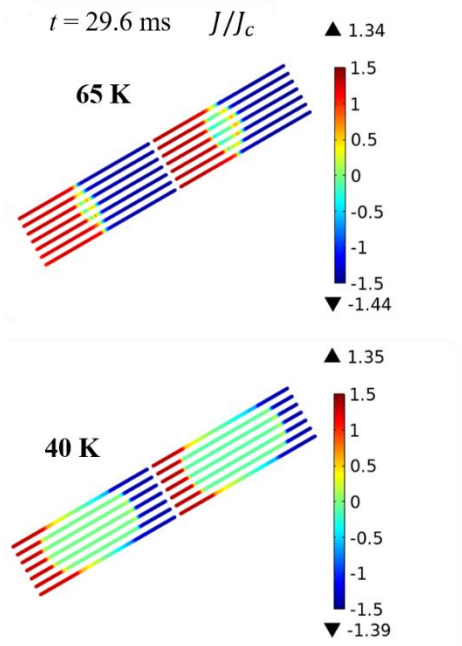

FIGURE 17. **Normalized current density J/J_c distributions in C1 wound with 4 mm-wide HTS conductor at operating temperature of 65 K and 40 K.**

C. INFLUENCE OF ASYMMETRIC $I_c(B,\theta)$ CHARACTERISTICS ON AC LOSS OF ARMATURE WINDINGS

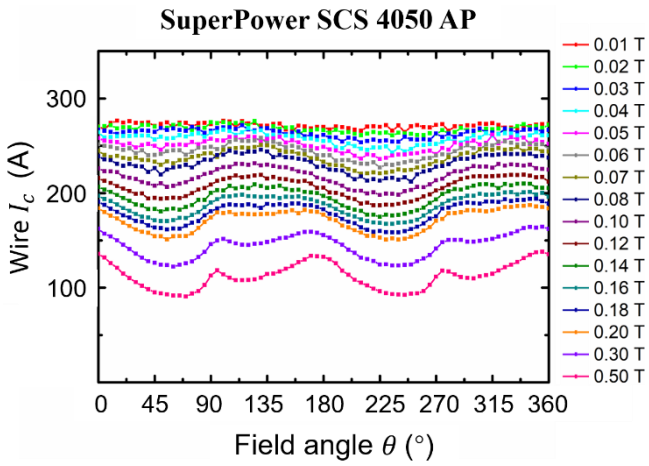

FIGURE 18. **The measured asymmetric $I_c(B, \theta)$ of a SuperPower SCS 4050 AP (RE)BCO conductor at 65 K.**

Fig. 18 shows the measured I_c (B, θ) of a 4 mm-wide SuperPower SCS 4050 AP (RE)BCO conductor in the full field range from 0° to 360° at 65 K [26], [29]. The I_c (B, θ) characteristics are highly asymmetric. The AC loss in the armature winding wound with the SuperPower conductor were calculated using the asymmetric I_c (B, θ) data for (a) non-flipped and (b) flipped conductor cases. Fig. 19 shows the schematics of the double racetrack coil flipping. Compared with the non-flipped coil, the field angle of the (RE)BCO conductors in the flipped coil changes to 180° - θ as shown previously in Fig. 1 (b). It is worth noting that the change of current direction is also considered in the resultant field angle [26].

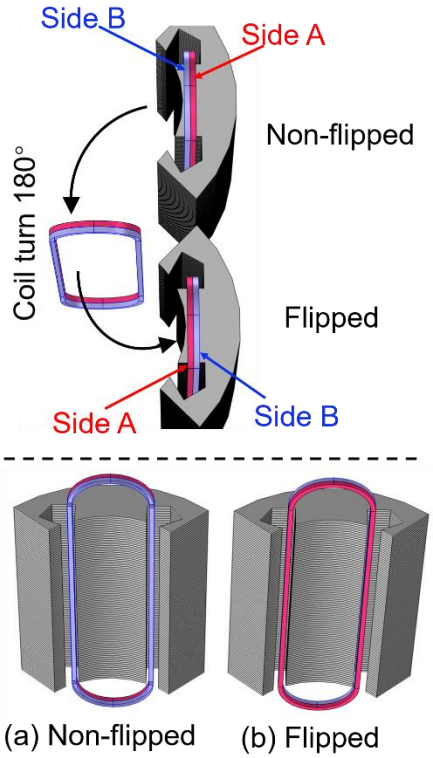

FIGURE 19. **Schematic drawing of the flipping of a double racetrack armature coil: (a) non-flipped; (b) flipped.**

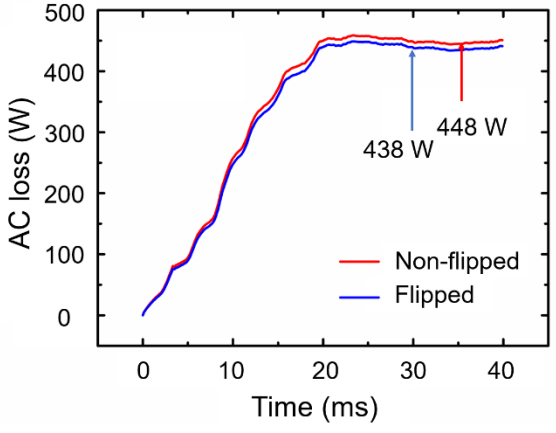

FIGURE 20. **Comparison of the average AC loss between non-flipped and flipped armature windings wound assuming the asymmetric $I_c(B, \theta)$ data of the SuperPower conductor.**

Fig. 20 shows the simulated AC loss in the non-flipped and flipped armature windings wound with the SuperPower conductor at 65 K plotted as a function of time. The average

AC loss in the entire non-flipped armature winding is 448 W while that in the entire flipped armature winding is 438 W. The 10 W AC loss reduction can be translated to approximately a 2% AC loss reduction. However, the AC loss reduction is achieved with minimal effort by simply flipping the coil winding. Furthermore, considering a cooling penalty of 20 at 65 K, the AC loss reduction is approximately 200 W if translated to room temperature. This is the first numerical demonstration of an AC loss reduction in a coil winding wound with a conductor with asymmetric I_c (B, θ) characteristics under a rotating magnetic field.

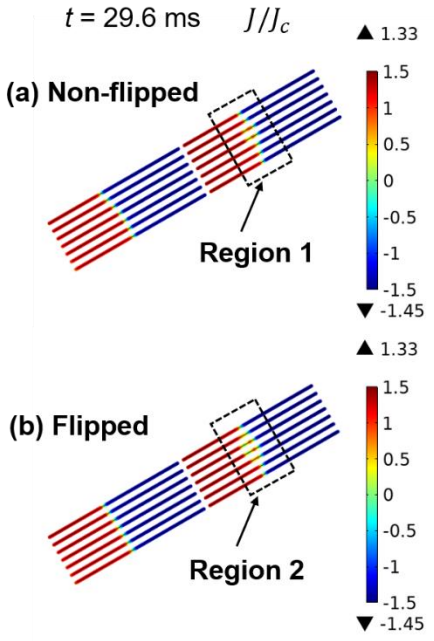

FIGURE 21. Normalized current density J/J_c distributions in C1 wound with the SuperPower conductor at t = 29.6 ms: (a) non-flipped and (b) flipped.

Fig. 21 shows the normalized current density J/J_c in C1 for the non-flipped and flipped cases. Even though the distributions for the two cases are similar, one can still notice that the current-free region in the flipped C1 is slightly larger than non-flipped one. This subtle difference means more flux penetration in the non-flipped case for these particular asymmetric I_c (B, θ) characteristics. This may explain the 2% AC loss difference for the two cases because the AC loss is generated primarily in the fully penetrated regions.

IV. CONCLUSION

In this work, we have numerically investigated the AC loss behaviour of the armature windings of an HTS motor wound with different types of (RE)BCO conductor arrangements at 65 K, wound with 4 mm-wide (RE)BCO conductor, 14/2 (14 strands, each strand is 2 mm wide) (RE)BCO Roebel cables; and striated (RE)BCO conductors with four 1 mm-wide filaments. Finite-element models implementing the ***T-A*** formulation and a rotating mesh were built using commercial FEM software COMSOL Multiphysics. The simulation results show that the AC loss in the armature winding wound with 4 mm-wide (RE)BCO conductor can be significantly reduced by utilising low-loss Roebel cables and striated conductors, where AC loss reductions of 30% and 58% were calculated for the Roebel cables and striated conductors, respectively. It is shown that the magnetization loss in the armature windings dominates the total AC loss and the AC loss reduction is mainly due to a reduction in magnetization loss values because of different flux penetration behaviour.

The temperature dependence of the AC loss in the armature winding wound with 4 mm-wide (RE)BCO conductor was also studied in the temperature range of 40 K - 65 K. The AC loss in the armature winding decreases with decreasing operating temperature. This AC reduction is attributed to the increase in the effective penetration field of the armature winding which is proportional to the critical current of the conductors that increases with decreasing operating temperatures.

Furthermore, the AC loss in an armature windings wound with a SuperPower SCS4050-AP (artificial pinning) wires which exhibit strongly asymmetric $I_c(B, \theta)$ characteristics are carried out to study the influence of the wire $I_c(B, \theta)$ on the AC loss in the HTS armature windings under rotating magnetic fields. The AC loss in the armature windings is reduced by 2% by simply flipping the direction of the armature coils. This is the first numerical demonstration of an AC loss reduction in a coil winding with a conductor with asymmetric $I_c(B, \theta)$ characteristics under a rotating magnetic field.

The simulation results in this work have practical implications for designing all-HTS superconducting rotating machines.

APPENDIX

Details about the calculation of the parameters in Table I is shown below.

Mutual inductance between field winding and phase A coil is calculated using the 2-D FEA (FEMM public) code. FEA codes provides flux linkages with phase A coil. On this basis, the mutual coupling between the field coil and stator Phase A coil is M_{af} = 12.6 μH/turn. The same number is obtained when stator coil is excited and mutual coupling with the field coil is calculated.

In our design, each field coil has 40 turns and each stator phase coil has 30 turns. Using these turns, the mutual reactance between the field and stator phase A coil is:

$$X_{af} = \omega \cdot M_{af} \cdot N_s \cdot N_f \ (\Omega)$$

where $\omega = 2 \cdot \pi \cdot f$ – rotational frequency
M_{af} = mutual inductance between field and phase A stator windings (H/turn)

N_a = number of turns in stator phase A
N_f = number of turns in field coil

Synchronous reactance (X_d) is determined similarly by just exciting the stator coils. Induced voltage in stator coils, $E = X_{af} \cdot I_f$, where I_f is field current.

Terminal voltage, $V_t = \sqrt{E^2 - (X_d \cdot I_a)^2}$, where I_a is phase A current (resistance of phase A is neglected).

RMS terminal voltage is $V_{rms} = V_t/\sqrt{2}$ and RMS phase A current $I_{rms} = I_a/\sqrt{2}$.

Power output for 3-phases $P_o = 3 \cdot V_{rms} \cdot I_{rms}$ by assuming power factor = 1.

P_o = 106 kW is obtained in our analysis.

ACKNOWLEDGMENT

This work was supported by the New Zealand Ministry of Business, Innovation and Employment (MBIE) under contract No. RTVU1707 and Strategic Science Investment Fund "Advanced Energy Technology Platforms" under contract No. RTVU2004. M D Ainslie is supported by an Engineering and Physical Sciences Research Council (EPSRC) Early Career Fellowship, EP/P020313/1. All data is provided in full in the results section of this paper.

REFERENCES

[1] B. B. Gamble, S. Kalsi, G. Snitchler, D. Madura, and R. Howard, "The status of HTS motors," in *IEEE Power Engineering Society Summer Meeting*, vol. 1, pp. 270–274, 2002, doi: 10.1109/PESS.2002.1043231.

[2] N. Amemiya, S. Murasawa, N. Banno, and K. Miyamoto, "Numerical modelings of superconducting wires for AC loss calculations," *Phys. C Supercond.*, vol. 310, no. 1, pp. 16–29, 1998, doi: https://doi.org/10.1016/S0921-4534(98)00427-4.

[3] Z. Hong, A. M. Campbell, and T. A. Coombs, "Numerical solution of critical state in superconductivity by finite element software," *Supercond. Sci. Technol.*, vol. 19, no. 12, pp. 1246–1252, 2006, doi: 10.1088/0953-2048/19/12/004.

[4] M. Zhang and T. A. Coombs, "3D modeling of high-T c superconductors by finite element software," *Supercond. Sci. Technol.*, vol. 25, no. 1, 2012, Art. no. 015009, doi: 10.1088/0953-2048/25/1/015009.

[5] V. M. R. Zermeño and F. Grilli, "3D modeling and simulation of 2G HTS stacks and coils," *Supercond. Sci. Technol.*, vol. 27, no. 4, 2014, Art. no. 044025, doi: 10.1088/0953-2048/27/4/044025.

[6] H. Zhang, M. Zhang, and W. Yuan, "An efficient 3D finite element method model based on the T-A formulation for superconducting coated conductors," *Supercond. Sci. Technol.*, vol. 30, no. 2, 2017, Art. no. 024005, doi: 10.1088/1361-6668/30/2/024005.

[7] C. Giuffrida, G. Gruosso, and M. Repetto, "Finite formulation of nonlinear magnetostatics with integral boundary conditions," *IEEE Trans. Magn.*, vol. 42, no. 5, pp. 1503–1511, 2006, doi: 10.1109/TMAG.2006.871543.

[8] P. Alotto, G. Gruosso, F. Moro, and M. Repetto, "A boundary integral formulation for eddy current problems based on the cell method," *IEEE Trans. Magn.*, vol. 44, no. 6, pp. 770–773, 2008, doi: 10.1109/TMAG.2007.916039.

[9] F. Moro, J. Smajic, and L. Codecasa, "A Novel h-φ approach for solving eddy-current problems in multiply connected regions," *IEEE Access*, vol. 8, pp. 170659–170671, 2020, doi: 10.1109/ACCESS.2020.3025291.

[10] R. Brambilla, F. Grilli, L. Martini, M. Bocchi, and G. Angeli, "A Finite-Element Method Framework for Modeling Rotating Machines with Superconducting Windings," *IEEE Trans. Appl. Supercond.*, vol. 28, no. 5, Aug. 2018, Art. no. 5207511, doi: 10.1109/TASC.2018.2812884.

[11] T. Benkel, M. Lao, Y. Liu, E. Pardo, S. Wolfstädter, T. Reis, and F. Grilli, "T-A-Formulation to Model Electrical Machines with HTS Coated Conductor Coils," *IEEE Trans. Appl. Supercond.*, vol. 30, no. 6, 2020, Art. no. 5205807, doi: 10.1109/TASC.2020.2968950.

[12] C. R. Vargas-Llanos, S. Lengsfeld, and F. Grilli, "T-A formulation for the design and AC loss calculation of a superconducting generator for a 10 MW wind turbine," *IEEE Access*, vol. 8, pp. 208767–208778, 2020, doi: 10.1109/ACCESS.2020.3038058.

[13] Y. Yang, H. Yong, X. Zhang, and Y. Zhou, "Numerical Simulation of Superconducting Generator Based on the T-A Formulation," *IEEE Trans. Appl. Supercond.*, vol. 30, no. 8, 2020, Art. no. 5207611, doi: 10.1109/TASC.2020.3005503.

[14] N. J. Long, R. A. Badcock, P. Beck, M. Mulholland, N. Ross, M. Staines, H. Sun, J. Hamilton, and R. G. Buckley, "Narrow strand YBCO Roebel cable for lowered AC loss," *J. Phys. Conf. Ser.*, vol. 97, no. 1, 2008, Art. no. 012280, doi: 10.1088/1742-6596/97/1/012280.

[15] S. Terzieva, M. Vojenčiak, E. Pardo, F. Grilli, A. Drechsler, A. Kling, A. Kudymow, F. Gömöry, and W. Goldacker, "Transport and magnetization ac losses of ROEBEL assembled coated conductor cables: measurements and calculations," *Supercond. Sci. Technol.*, vol. 23, no. 1, 2009, Art. no. 014023, doi: 10.1088/0953-2048/23/1/014023.

[16] Z. Jiang, R. A. Badcock, N. J. Long, M. Staines, K. P. Thakur, L. S. Lakshmi, A. Wright, K. Hamilton, G. N. Sidorov, R. G. Buckley, N. Amemiya, and A. D. Caplin, "Transport AC loss characteristics of a nine strand YBCO Roebel cable," *Supercond. Sci. Technol.*, vol. 23, no. 2, 2010, Art. no. 025028, doi: 10.1088/0953-2048/23/2/025028.

[17] N. J. Long, R. A. Badcock, K. Hamilton, A. Wright, Z. Jiang, and L. S. Lakshmi, "Development of YBCO Roebel cables for high current transport and low AC loss applications," *J. Phys. Conf. Ser.*, vol. 234, no. 2, 2010, Art. no. 022021, doi: 10.1088/1742-6596/234/2/022021.

[18] W. Goldacker, F. Grilli, E. Pardo, A. Kario, S. I. Schlachter, and M. Vojenčiak, "Roebel cables from REBCO coated conductors: A one-century-old concept for the superconductivity of the future," *Supercond. Sci. Technol.*, vol. 27, no. 9, 2014, Art. no. 093001, doi: 10.1088/0953-2048/27/9/093001.

[19] C. B. Cobb, P. N. Barnes, T. J. Haugan, J. Tolliver, E. Lee, M. Sumption, E. Collings, and C. E. Oberly, "Hysteretic loss reduction in striated YBCO," *Phys. C Supercond. its Appl.*, vol. 382, no. 1, pp. 52–56, 2002, doi: 10.1016/S0921-4534(02)01196-6.

[20] N. Amemiya, S. Kasai, K. Yoda, Z. Jiang, G. A. Levin, P. N. Barnes, and C. E. Oberly, "AC loss reduction of YBCO coated conductors by multifilamentary structure," *Supercond. Sci. Technol.*, vol. 17, no. 12, pp. 1464–1471, 2004, doi: 10.1088/0953-2048/17/12/018.

[21] G. A. Levin, P. N. Barnes, N. Amemiya, S. Kasai, K. Yoda, and Z. Jiang, "Magnetization losses in multifilament coated superconductors," *Appl. Phys. Lett.*, vol. 86, no. 7, 2005, Art. no. 072509, doi: 10.1063/1.1861955.

[22] J. Šouc, F. Gömöry, J. Kováč, R, Nast, A. Jung, M. Vojenčiak, F. Grilli, and W. Goldacker, "Low AC loss cable produced from transposed striated CC tapes," *Supercond. Sci. Technol.*, vol. 26, no. 7, 2013, Art. no. 075020, doi: 10.1088/0953-2048/26/7/075020.

[23] F. Grilli and A. Kario, "How filaments can reduce AC losses in HTS coated conductors: a review," *Supercond. Sci. Technol.*, vol. 29, no. 8, 2016, Art. no. 083002, doi: 10.1088/0953-2048/29/8/083002.

[24] Z. Hong, W. Li, Y. Chen, F. Gömöry, L. Frolek, M. Zhang, and J. Sheng, "Design optimization of superconducting coils based on asymmetrical characteristics of REBCO tapes," *Phys. C Supercond.*, vol. 550, pp. 74–77, 2018, doi: 10.1016/j.physc.2018.04.008.

[25] Z. Jiang, N. Endo, S. C. Wimbush, J. Brooks, W. Song, R. A. Badcock, D. Miyagi, and M. Tsuda, "Exploiting asymmetric wire critical current for the reduction of AC loss in hts coil windings," *J. Phys. Commun.*, vol. 3, no. 9, 2019, Art. no. 095017, doi: 10.1088/2399-6528/ab4437.

[26] Z. Jiang, W. Song, X. Pei, J. Fang, R. A. Badcock, and S. C. Wimbush, "15% reduction in AC loss of a 3-phase 1 MVA HTS transformer by exploiting asymmetric conductor critical current," *J. Phys. Commun.*, vol. 5, no. 2, 2021, Art. no. 025003, doi: 10.1088/2399-6528/ABE036.

[27] I. Kesgin, G. Majkic, and V. Selvamanickam, "Fully filamentized HTS coated conductor via striation and selective electroplating," *Phys. C Supercond.*, vol. 486, pp. 43–50, 2013, doi: https://doi.org/10.1016/j.physc.2013.01.016.

[28] J. Rhyner, "Magnetic properties and AC-losses of superconductors with power law current—voltage characteristics," *Phys. C Supercond.*, vol. 212, no. 3, pp. 292–300, 1993, doi: https://doi.org/10.1016/0921-4534(93)90592-E.

[29] S. C. Wimbush and N. M. Strickland, "A Public Database of High-Temperature Superconductor Critical Current Data," *IEEE Trans. Appl. Supercond.*, vol. 27, no. 4, 2017, Art. no. 8000105, doi: 10.1109/TASC.2016.2628700.

[30] Z. Jiang and N. Amemiya, "Comparison of the total AC loss characteristics in YBCO conductors and BSCCO multifilamentary tapes with identical engineering critical current densities," *Supercond. Sci. Technol.*, vol. 19, no. 8, pp. 742–747, 2006, doi: 10.1088/0953-2048/19/8/009.

[31] N. Amemiya, T. Nishioka, Z. Jiang, and K. Yasuda, "Influence of film width and magnetic field orientation on AC loss in YBCO thin film," *Supercond. Sci. Technol.*, vol. 17, no. 3, pp. 485–492,

2004, doi: 10.1088/0953-2048/17/3/031.

[32] E. H. Brandt and M. V Indenbom, "Type-II-superconductor strip with current in a perpendicular magnetic field," *Phys. Rev. B.*, vol. 48, no. 17, pp. 12893–12906, Nov. 1993, doi: 10.1103/PhysRevB.48.12893.

[33] M. Iwakuma, K. Toyota, M. Nigo, T. Kiss, K. Funaki, Y. Iijina, T. Saitoh, Y. Yamada, and Y. Shiohara, "AC loss properties of YBCO superconducting tapes fabricated by IBAD–PLD technique," *Phys. C Supercond.*, vol. 412–414, pp. 983–991, 2004, doi: https://doi.org/10.1016/j.physc.2004.01.112.

[34] Z. Jiang, N. Amemiya, K. Kakimoto, Y. Iijima, T. Saitoh, and Y. Shiohara, "The dependence of AC loss characteristics on the space in stacked YBCO conductors," *Supercond. Sci. Technol.*, vol. 21, no. 1, 2008, Art. no. 015020, doi: 10.1088/0953-2048/21/01/015020.

Shuangrong You received the M.S. degree in condensed matter physics from the Shanghai University, Shanghai, China, in 2018. He is currently pursuing a Ph.D. degree at Robinson Research Institute, Victoria University of Wellington.

His current research interests include high-temperature superconducting (HTS) rotating machines, AC loss research in HTS coils and devices, numerical modelling for HTS devices.

Dr. Swarn Kalsi (Life Fellow, IEEE) has over fifty years of experience in all aspects of electrical engineering and electric equipment design and development. During his long career, he has designed, built, tested, and performed system simulation studies for equipment such as rotating machines, fault current limiters, transformers, power transmission cables, fusion and Maglev train systems.

All his academic background is in area of electrical power equipment. He received his B.S. and M.S. degrees from Indian Institute of Technology of Kharagpur and Varanasi, and Ph.D. degree from Imperial College, London.

Since 2007, he is helping international clients for designing rotating machines for a variety of applications, such as high-speed machines for aerospace and slow speed machines for wind turbine and ship propulsion, and superconducting power cables, transformers, and fault current limiters.

Prior to this he had worked various positions with American Superconductors (15 yr), Northrop Grumman (10 yr), General Electric (15 yr). During these periods, he developed superconductor applications for electric power equipment, fusion magnets, Maglev prototype and accelerators.

He has numerous publications and patents to his credit.

Mark D. Ainslie (Senior Member, IEEE) received the B.E. (Electrical & Electronic) & B.A. (Japanese) degree in from the University of Adelaide, Australia, in 2004, the M.Eng. degree from the University of Tokyo, Japan, in 2008, and the Ph.D. degree from the University of Cambridge, UK, in 2012. From 2012 to 2017, he was a Royal Academy of Engineering Research Fellow in the Bulk Superconductivity Group at the University of Cambridge, and since July 2017, he has been an EPSRC Early Career Fellow, in the same research group, as the principal investigator of a project investigating the use of bulk HTS materials in portable high field magnet systems. He has published over 100 peer-reviewed articles covering a broad range of topics in applied superconductivity from fundamental materials science to numerical modelling to application design and testing.

Rodney A. Badcock (SM'18) received the B.Sc. degree in physics with electronics from the University of Leeds, Leeds, U.K., and the M.Sc. and Ph.D. degrees in manufacturing and materials engineering from Brunel University, England, U.K. He has 30 years research experience in applied R&D covering manufacturing process monitoring and control, materials sensing, and superconducting systems. Since 2006, he has concentrated on superconducting machines, and production and machines for General Cable Superconductors at the Robinson Research Institute, Victoria University of Wellington, Lower Hutt, New Zealand. He is currently the Institute Deputy Director, Chief Engineer, Professor and specializes in the management of complex engineering projects, including customer-focused multidisciplinary projects. He is particularly known for the development of the superconducting dynamos for electric machines and the NZ MBIE programme developing aircraft superconducting electric propulsion technology. Rod is recognized as one of the leading experts in the application of superconducting dynamos and cables to electric machines.

Dr. Badcock was a key member of the team awarded the Royal Society of New Zealand Cooper Medal in 2008 for the development of high-temperature superconducting cables for power system applications including 1 MVA transformer, 60 MW hydro generator, and 150 MW utility generator.

Prof. Nicholas J. Long is Director of the Robinson Research Institute, Victoria University of Wellington, New Zealand. He obtained a MSc in Physics at Victoria University and completed a PhD in Physics at the University of Southern California. From 1994 -2013 he worked at Industrial Research Ltd (IRL). His primary research has been in high temperature superconductivity (HTS). He was a founder of the program at IRL to develop HTS Roebel cables. His other HTS work has focussed on enhancing wire performance and understanding the phenomenology of critical currents. More recent projects involve the application of superconductivity to satellite and space technology.

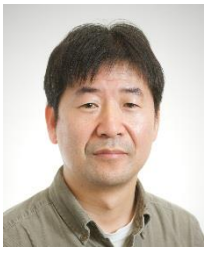

Zhenan Jiang (Senior Member, IEEE) received a B.Eng. in Electrical Engineering from Chongqing University in Chongqing, China in 1994, and M.Eng., Ph.D. Eng. in applied superconductivity from Yokohama National University in Yokohama, Japan in 2002 and 2005, respectively.

He was a Postdoctoral Research Fellow at Yokohama National University from 2005 to 2008. He joined the

Superconductivity Group currently known as the Robinson Research Institute at Victoria University of Wellington, New Zealand in 2008 as Research Scientist. He has a strong track record in characterization of high temperature superconductors (HTS), especially in AC loss and has published more than 100 peer-reviewed journal papers. He is now Principal Scientist in the institute. His recent research interests include AC loss characterization in HTS, HTS applications including transformers, flux pumps, magnets, and rotating machines.

Dr. Jiang has been twice awarded the JSPS (Japan Society for the Promotion of Science) invitation fellowship to Kyoto University under the NZ-Japan Scientist Exchange Program, in 2011 and 2015, respectively. He is an editorial board member of *Superconductivity*, an Elsevier journal established in September 2021.